

Optical excitation of valley and spin currents of chiral edge states in graphene with Rashba spin-orbital coupling

Ma Luo* and Zhibing Li

The State Key Laboratory of Optoelectronic Materials and Technologies, School of Physics, Sun Yat-Sen University, Guangzhou 510275, People's Republic of China

(Received 19 June 2017; revised manuscript received 25 August 2017; published 13 October 2017)

Graphene on a substrate with a topological line defect possesses chiral edge states that exhibit linear dispersion and have opposite Fermi velocities for two valleys. The chiral edge states are localized at the line defect. With the presence of Rashba spin-orbital coupling, the dispersion of the chiral edge states splits into two. The optical excitation is modeled by the generalized semiconductor Bloch equation based on tight-binding theory. Charge, valley, and spin currents generated by normally incident plane waves through the photogalvanic effect as well as those generated by oblique light through the surface-plasmon drag effect are studied. Conditions for optical generation of purely localized valley or spin currents, which are solely originated from the chiral edge states, are discussed.

DOI: [10.1103/PhysRevB.96.165424](https://doi.org/10.1103/PhysRevB.96.165424)

I. INTRODUCTION

Spintronics [1] has been studied for decades. In recent years, it has been generalized to the pseudospin degrees of freedom associated with degenerating minima of the electron energy bands and is called valleytronics [2]. Optical generation of spin and valley currents is essential for integration of spintronic and valleytronic nanodevices for optical communication [3]. Graphene has small intrinsic spin-orbital coupling and long spin-diffusion length, and therefore is a promising material for spintronic nanosystems [4–6]. In addition, the band structure of graphene has two separating inequivalent valleys at the Fermi level, which is suitable for valleytronic physics [7,8]. Recent researches have been devoted to explore optical excitation of spin [9–12] and valley [13,14] currents in graphene and graphenelike materials. The edge states of graphene support localized spin and charge currents that would lead to novel spintronic and valleytronic devices. The domain wall in gapped graphene supports localized edge states [15], the band structure of which exhibits chirality [16]. This paper theoretically explores the optical excitation of the chiral edge states of graphene [16–20] on a conformal substrate, and the generation of the localized spin and valley currents.

The A sublattice and the B sublattice of graphene on the hexagonal boron-nitride (h-BN) or SiO₂ substrate have different potentials. A band gap is thereby induced and excitations are described by the massive Dirac fermion [21,22]. A topological line defect of the substrate, as shown in Fig. 1(a), separates the ribbon of graphene into two regions with opposite local potentials for the A and B lattice sites. Thus, the mass of the Dirac fermion changes sign as it crosses the defect line. For each region, the sign of the mass has no effect on the band structure and wave functions. However, at the interface of two regions where the mass term flips sign, chiral edge states with linear dispersion near to the Fermi level can be formed [16,18]. The slopes of the dispersion at K and K' valleys are opposite to each other. Chiral edge states are found to be robust even in case of a nonperfect line defect.

This paper investigates the band structure and wave functions of the chiral edge states in the presence of Rashba spin-orbital coupling (SOC) [23–25]. The optical excited population distribution at the chiral edge bands and the bulk bands leads to charge current and spin current at each valley. Since chiral edge states are localized near to the interface, they carry localized charge and spin currents. We calculate the charge, valley, and spin currents generated by normal incident plane waves with linear and circular polarization, as well as those generated by the evanescent wave of the surface plasmon (SP) excited by oblique incident light [26].

The paper is organized as follows. Section II describes the physical system that supports chiral edge states and enables optical excitation. The chiral edge states are calculated in two ways: with the continuous Dirac fermion model as well as with the discrete tight-binding model. Section III is devoted to optically induced charge, valley, and spin currents at variant parameters. Two systems that would support the desired optical generation of localized valley and spin currents are discussed. The conclusion is given in the last section.

II. SYSTEM AND MODEL

A. Description of the system

The basic structure to sustain optical generation of lined localized spin current and valley current consists of a nanoribbon of graphene on top of the h-BN substrate, as shown in Fig. 1(a). Graphene is on the x - y plane, with a zigzag edge parallel to the y direction. A topological line defect along the y axis separates the substrate into two regions. In one region, boron atoms (nitride atoms) locate at the A (B) sites of the hexagonal lattice, and vice versa in the other region. Because h-BN is a wide-band-gap semiconductor, the optical effect at low frequency is negligible. The h-BN substrate induces a sublattice dependent potential which breaks the symmetry between the A sublattice and B sublattice of graphene, and thereby opens band gaps in two Dirac cones and generates the mass of the Dirac fermion. Although the band structures of the massive Dirac fermion in two regions are the same, the interface between them supports chiral edge states, which are

*luom28@mail.sysu.edu.cn

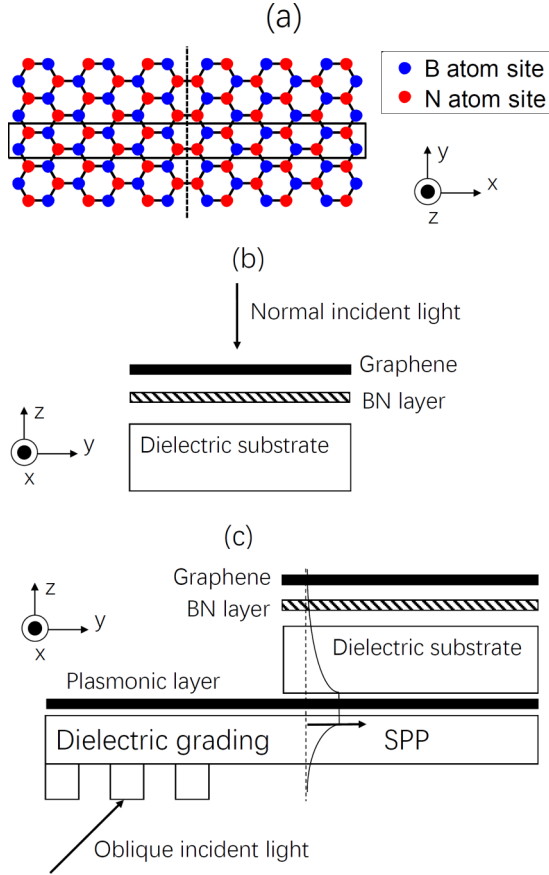


FIG. 1. (a) Top view of the graphene nanoribbon on the h-BN substrate. The lattice sites on top of the boron and nitride atom are represented by the blue (dark) and red (gray) circles, respectively. The dashed line indicates the location of the topological line defect along the zigzag edge. The rectangle is the supercell for the tight-binding calculation. (b) Side view of the system sustaining the photogalvanic effect. (c) Side view of the system sustaining the surface-plasmon drag effect.

localized near to the interface [16]. A vertical static electric field along the z direction induces Rashba SOC in the graphene,

which splits the band of the chiral edge states, as shown in the later part of this paper.

For a practical design of an optical device, the graphene-on-h-BN layer is deposited on top of a dielectric substrate. The vertical static electric field can be applied by adding a gate voltage to a transparent electrode on top of graphene with the dielectric substrate earthed. Figure 1(b) shows the system for optical generation of currents by the photogalvanic effect, where the normally incident optical light excites the chiral edge states as well as bulk states. Figure 1(c) shows the system for optical generation of currents by the surface-plasmon drag effect. The obliquely incident optical field in the dielectric grading excites SPs in the plasmonic layer, and the evanescent waves of the SPs excite the Dirac fermions in graphene with large momentum transfer.

The quantum states in graphene near to the Fermi level can be described either by the continuous Dirac equation or more precisely by the discrete tight-binding model. The solution to the Dirac equation can provide more transparent insight into the physical property of the chiral edge states. Meanwhile, the discrete model provides a more precise numerical solution. We first solve the Dirac equation to find the solution of the chiral edge states with Rashba SOC, and then solve the same problem with the discrete tight-binding model. The band structure and the wave functions obtained from two methods will be compared. In addition, the description of the interaction with external optical field based on the discrete tight-binding model is given.

B. Chiral edge states with Rashba SOC: Continuous model

In the continuous model, the Rashba SOC is given by $H_R = \hbar\Omega_R \hat{z} \cdot (\vec{\sigma} \times \mathbf{S})$, where Ω_R is the Rashba SOC strength, and $\vec{\sigma}$ and \mathbf{S} are the vectors of the Pauli matrices of pseudospin and real spin, respectively [9,10]. The Rashba SOC strength Ω_R is proportional to the vertical static electric field [25], and could be enhanced by varying types of metal-atom absorption on graphene [27–29]. Throughout this paper, the Rashba SOC strength takes the typical value $\hbar\Omega_R = 12$ meV. In the direct product space of the pseudospin and real spin, $[\psi_{A\uparrow}, \psi_{B\uparrow}, \psi_{A\downarrow}, \psi_{B\downarrow}]^T$, the matrix expression of the Hamiltonian is given as

$$H = \begin{bmatrix} \Delta(x) & -i\hbar v_F(\tau\partial_x - i\partial_y) & 0 & i\hbar\Omega_R(-\tau + 1) \\ -i\hbar v_F(\tau\partial_x + i\partial_y) & -\Delta(x) & i\hbar\Omega_R(-\tau - 1) & 0 \\ 0 & i\hbar\Omega_R(\tau + 1) & \Delta(x) & -i\hbar v_F(\tau\partial_x - i\partial_y) \\ i\hbar\Omega_R(\tau - 1) & 0 & -i\hbar v_F(\tau\partial_x + i\partial_y) & -\Delta(x) \end{bmatrix} \quad (1)$$

where v_F is the Fermi velocity of graphene, $\Delta(x) = \Delta_0 x/|x|$ is the equivalent mass induced by the h-BN substrate, and τ is equal to ± 1 for K and K' valleys, respectively. The h-BN substrate induces a gap of $2\Delta_0 = 56$ meV, which has been confirmed by theoretical calculation [30] and experimental observation [22]. In the homogeneous regions on the left ($x < 0$) and on the right ($x > 0$), the plane waves can be written as $\Psi(k_x, k_y) = [\psi_{A\uparrow}, \psi_{B\uparrow}, \psi_{A\downarrow}, \psi_{B\downarrow}]^T e^{i(k_x x + k_y y)}$. Inserting this into the Dirac equation with Hamiltonian (1), the dispersion relation of the traveling plane waves is

$$\epsilon_{\pm}^2(k_x, k_y) = \Delta_0^2 + \frac{(\hbar\Omega_R)^2}{2} + (\hbar v_F k_x)^2 + (\hbar v_F k_y)^2 \pm \frac{\hbar\Omega_R}{2} \sqrt{(\hbar\Omega_R)^2 + (2\hbar v_F k_x)^2 + (2\hbar v_F k_y)^2} \quad (2)$$

where \pm stand for two spin states from the SOC energy splitting. With the presence of the line defect, the bulk states consist of incident, transmission, and reflection traveling plane waves of the Dirac fermion. The scattering of an incident plane wave by the line defect along the y axis produces two transmission and two reflection plane waves with the same energy and the same k_y , but different k_x . As a result, the quantum states of the two bands, ϵ_+ and ϵ_- , are mixed. The scattering coefficients can be calculated by matching the solutions at the interface. It is more convenient for the investigation of the scattering process to write the dispersion relation as

$$(\hbar v_F k_{x\pm})^2 = \epsilon^2 - \Delta_0^2 \pm \hbar \Omega_R \sqrt{\epsilon^2 - \Delta_0^2} - (\hbar v_F k_y)^2. \quad (3)$$

Although this expression is implicit for the energy level, it is explicit for the wave number k_x and k_y . Because the scattering by the line defect preserves ϵ and k_y , Eq. (3) directly gives the two $k_{x\pm}$ corresponding to the two scattering plane waves.

The localized chiral edge states caused by the line defect are traveling waves along the y axis and exponentially decay in both positive and negative x directions. Making the replacement $k_{x\pm} = i\gamma_{\pm}$, the basic solutions at $x > 0$ and $x < 0$ regions become $\Psi(\gamma_{\pm}, k_y) = [\psi_{A\uparrow}, \psi_{B\uparrow}, \psi_{A\downarrow}, \psi_{B\downarrow}]^T e^{ik_y y} e^{-\gamma_{\pm}|x|}$. The decay factor is obtained from Eq. (3) as

$$(\hbar v_F \gamma_{\pm})^2 = -\epsilon^2 + \Delta_0^2 \pm \hbar \Omega_R \sqrt{\epsilon^2 - \Delta_0^2} + (\hbar v_F k_y)^2. \quad (4)$$

The wave function is physically valid when $\text{Re}[\gamma_{\pm}] > 0$. When $\epsilon^2 < \Delta_0^2$, γ_{\pm} are complex and conjugate to each other. When $\Delta_0^2 < \epsilon^2 < \epsilon_{\pm}^2(0, k_y)$, the two solutions of γ_{\pm} are real with different magnitudes. The wave function at the left (right) half plane is the superposition of the two decaying basic solutions as $A_{L(R)}\Psi(\gamma_+, k_y) + B_{L(R)}\Psi(\gamma_-, k_y)$. Matching each component of the wave functions of two regions at the interface (at $x = 0$) leads to the equation for the eigenenergies:

$$4\epsilon^2\gamma_+\gamma_- - 4\Delta_0(\gamma_+ + \gamma_-)\tau k_y\epsilon + \Delta_0^2[(\gamma_+ - \gamma_-)^2 + 4k_y^2] = 0. \quad (5)$$

This equation is only valid outside of the band edges of the conduction and valence bands, $\epsilon^2 < \epsilon_{\pm}^2(0, k_y)$. When $\Omega_R = 0$, the exact solution of Eq. (5) is $\epsilon = \tau k_y$, which is twofold degenerate for chiral edge states with spin up and spin down. All spinor components of an edge state have an exponential factor $e^{-\Delta_0|x|/(\hbar v_F)}$. When Ω_R is nonzero, Eq. (5) is not quadratic and thus requires numerical calculation. The Rashba SOC mixes the chiral edge states with spin up and spin down, which splits the degenerated chiral bands into two splitting chiral bands, as shown in Fig. 2(a). The upper chiral band (indicated by the red circle line) asymptotically approaches the valence-band edge at $k_y \rightarrow -\infty$, and merges with the conduction-band edge at certain energy level ϵ_c , as indicated by the vertical downward arrow in the figure. This chiral band does not exist at $\epsilon > \epsilon_c$. The lower chiral band has similar properties as shown in the figure. The band structure of the chiral edge states in the K' valley can be obtained by the mirror reflection $k_y \rightarrow -k_y$ of that in the K valley.

The wave function of a typical chiral edge state, pointed out by the horizontal arrow in Fig. 2(a), is plotted in Fig. 3(a). A $\pi/2$ phase shift exists between the pseudospinor components

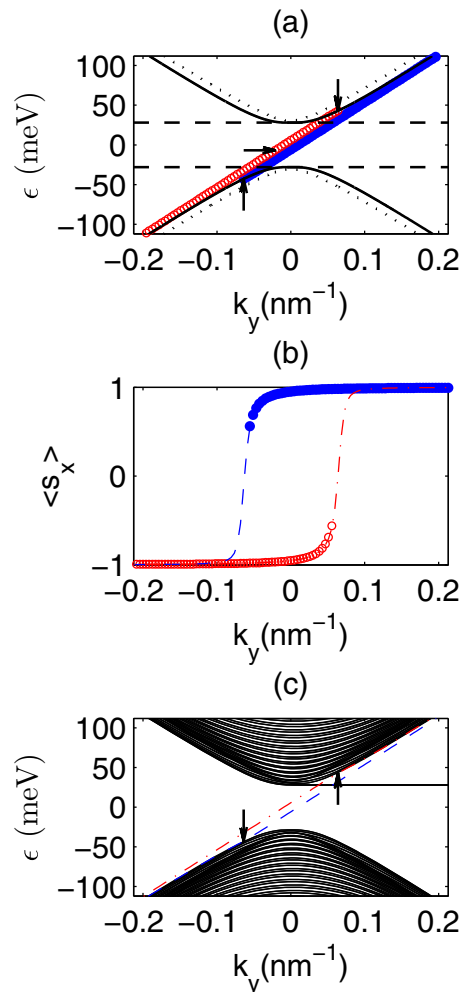


FIG. 2. (a) Band structure of the chiral edge states in the K valley ($\tau = 1$), which is calculated by the Dirac fermion model. The red (filled) and blue (empty) dots indicate the upper and lower branches of the chiral edge states. The solid (dotted) lines are the band edge of the first (second) conduction and valence bands, i.e., $\epsilon_-(0, k_y)$ [$\epsilon_+(0, k_y)$]. The dashed lines indicate the band gap of the bulk region. (b) The expectation values of spin x of the corresponding chiral edge states. The red (filled) and blue (empty) dots are calculated with the continuous Dirac fermion model. The red (dash-dotted) and blue (dashed) lines are calculated with the discrete tight-binding model. (c) The band structure of the nanoribbon with the topological line defect in the middle, which is calculated with the tight-binding theory.

of the A and B lattice sites, and a π phase shift exists between real spin-up and spin-down components. The real spin-up components have larger magnitudes than that of the real spin-down components in the $x > 0$ region, and vice versa. Although nonvisible in the figure, the wave functions of all four components have periodic nodes, because γ_{\pm} are conjugate to each other and the wave function $A_{L(R)}\Psi(\gamma_+, k_y) + B_{L(R)}\Psi(\gamma_-, k_y)$ contains a trigonometric function. Locations of the nodes of the four spinor components are different. The spatial distribution of the total density of probability $|\Psi|^2$ is symmetric at $x \rightarrow -x$ and exponentially decays without any node. The spatial distributions of expectations of the real spin along three spatial directions are calculated and plotted in

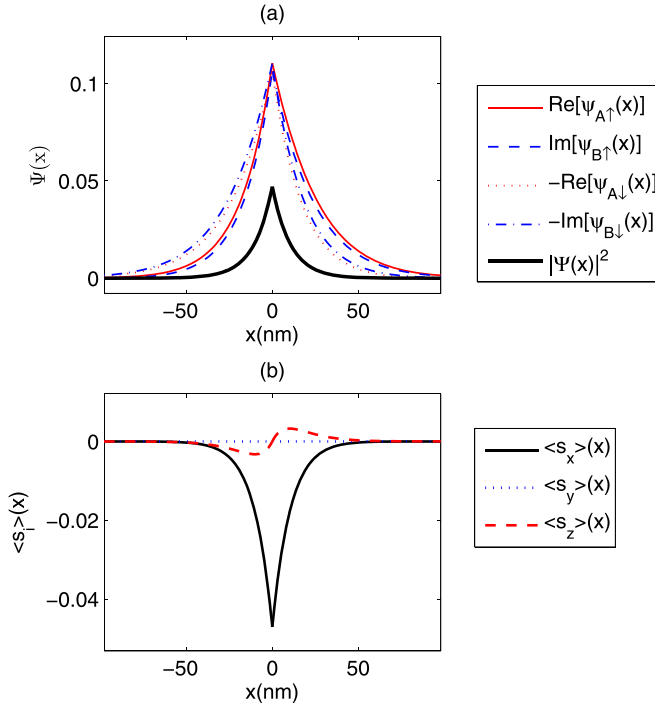


FIG. 3. The wave function and spin distribution of a specific chiral edge state indicated by the horizontal arrow in Fig. 2(a). (a) The wave function of each spinor component and the modulus of the wave function. (b) The expectation value of spin x , y , and z vs position x .

Fig. 3(b). The spin x has net magnitude, the spin y is zero everywhere, and the spin z has opposite sign in the left and right regions. The wave functions and spin distributions of the chiral edge states with $|\epsilon| < \Delta_0$ have the same properties. The wave functions of other chiral edge states with $|\epsilon| > \Delta_0$ also have similar properties, except that the wave function of each spinor component has at most one node, because both γ_{\pm} are real. The total spins x of all chiral edge states are calculated and plotted in Fig. 2(b). The spin x components of the two chiral bands have opposite signs.

C. Quantum states and optical excitation: Tight-binding model

In addition, to calculate with the continuous Dirac fermion model, we also perform calculations in the framework of the discrete tight-binding model. The unit cell of the tight-binding model is indicated in Fig. 1(a) as a solid box. The unit cell contains 4800 carbon atoms, having open boundary zigzag edges on the left and right. The topological line defect in the middle is 255.6 nm away from the edge. As a result, the edge effect could be neglected. The tight-binding Hamiltonian [24,25,31]

$$H = t \sum_{(i,j)\alpha} c_{i\alpha}^{\dagger} c_{j\alpha} + \sum_{i\alpha} \Delta(i) c_{i\alpha}^{\dagger} c_{i\alpha} + \frac{i\hbar\Omega_R}{3\sqrt{3}a_{C-C}} \sum_{(i,j),\alpha,\beta} c_{i\alpha}^{\dagger} [(\mathbf{S} \times \mathbf{d}_{ij}) \cdot \hat{\mathbf{z}}]_{\alpha\beta} c_{j\beta} \quad (6)$$

where $t = 2.8$ eV is the hopping energy, a_{C-C} is the bond length between the two nearest-neighbor carbon atoms, i and

j are the indices of lattice sites, α and β take values of ± 1 for spin up and spin down, $c_{i\alpha}^{\dagger}$ and $c_{i\alpha}$ are the creation and annihilation operators of the π electron with spin α and being located at lattice site i , \mathbf{S} is the vector of the Pauli matrix for real spin, and \mathbf{d}_{ij} is the vector from lattice i to j . The first summation runs over the nearest-neighbor sites $\langle i, j \rangle$ with the same spin index α ; the second summation runs over all lattice sites and spin indices; and the third summation runs over $\langle i, j \rangle$ and the two spin indices, α and β . The periodical boundary condition is applied along the y direction, with the Bloch phase being $K_y + k_y$ and $K'_y + k_y$ for the eigenstates in K and K' valleys, respectively, where $K_y = 2\pi/(3\sqrt{3}a_{C-C})$ and $K'_y = -2\pi/(3\sqrt{3}a_{C-C})$, and $k_y \in [-0.2, 0.2] \text{ nm}^{-1}$. The numerical diagonalization of Hamiltonian Eq. (6) gives the band structure of the nanoribbon, including the chiral bands, edge bands, and bulk bands, which is plotted in Fig. 2(c). Only the band structure near to the K valley is shown. Because the zigzag edge line defect does not induce intervalley scattering, the band structure near to the K' valley is related to that near to the K valley by the mirror reflection $k_y \rightarrow -k_y$. The chiral bands are the same as that from the continuous Dirac equation as shown in Fig. 2(a). The bulk bands, including the conduction and valence bands, are above and below the band edges as, respectively, shown with solid and dotted lines in Fig. 2(a). The tight-binding wave functions of the chiral edge states decay exponentially with the distance away from the line defect. On the other hand, the bulk states in the conduction and valence bands are traveling waves with transmission and reflection at the defect line. The upper (lower) branch of the chiral band goes into the conduction (valence) band at the point indicated by the upward (downward) arrow in Fig. 2(c). Within the bulk band, the chiral edge states are mixed with the bulk states and the wave functions have features of both exponentially decaying function and traveling wave. The energy levels of these quantum states are above (below) the conduction-band (valence-band) edge, and thus cannot be calculated by solving Eq. (5). There are additional edge states at the open boundary zigzag edge with energy level Δ_0 . Because the spatial overlap between the open boundary edge states and the chiral edge states is small, we neglect the edge states of the open boundaries in the calculation of the optical excitation. The expectation values of total spin x of the chiral bands are calculated by the tight-binding model as well, which are plotted in Fig. 2(b) and are the same as the results given by the continuous Dirac fermion model.

Interaction of the quantum states with external optical field is described by the tight-binding model with an interaction Hamiltonian. The optical field at the graphene plane can be expressed as $\mathbf{E}(\mathbf{r}, t) = \mathbf{E}_0 e^{i\mathbf{q}\cdot\mathbf{r} - i\omega t} + \text{c.c.}$, with \mathbf{E}_0 being the amplitude of the electric field, \mathbf{q} being the wave vector of the optical field in the graphene plane, and ω being the frequency of the incident field. The interaction Hamiltonian between the quantum states and the electric field is given by [26]

$$H_I = \sum_{(i,j)\alpha} M_{ij} c_{i\alpha}^{\dagger} c_{j\alpha} \quad (7)$$

where $M_{ij} = \frac{mc - \hbar e_0}{2m_0\omega} \hat{\mathbf{d}}_{ij} \cdot \mathbf{E}[(\mathbf{r}_i + \mathbf{r}_j)/2, t]$, e_0 is the charge of an electron, m_0 is the mass of an electron, $\hat{\mathbf{d}}_{ij}$ is the

unit vector along \mathbf{d}_{ij} , and $m_{C-C} = \int d\mathbf{r} \phi^*(\mathbf{r} + a_{C-C}\hat{x}) \hat{x} \cdot \nabla \phi(\mathbf{r}) \approx 3 \text{ nm}^{-1}$ is the matrix element of the momentum operator with $\phi(\mathbf{r})$ being the wave function of the π electron [32–34]. The matrix form of the interaction Hamiltonian is calculated, under the basis of the noninteracting tight-binding eigenstates of the Hamiltonian Eq. (6). Thus, the matrix elements of H_I are given as $H_{I,k_y n, k'_y n'} = \langle k_y n | H_I | k'_y n' \rangle$, with $|k_y n\rangle$ being the eigenstates of the Hamiltonian Eq. (6). Since the eigenstates of Eq. (6) do not conserve k_x and σ_z , the eigenstates with the same quantum number k_y are subscripted by a numerical index n . The optical field contains oscillation terms with positive and negative frequency, therefore the interaction Hamiltonian can be written as

$$H_I = \sum_{\kappa=\pm 1} H_I^\kappa e^{-i\kappa\omega t}. \quad (8)$$

Because the system preserves the lattice translational symmetry along the y direction, and the positive (negative) frequency oscillation term of the optical field includes the spatial phase factor $e^{iq_y y} (e^{-iq_y y})$, the matrix elements of the interaction Hamiltonian $\langle k_y n | H_I^\kappa | k'_y n' \rangle \propto \delta(-k_y + k'_y + \kappa q_y)$.

In the remaining part of the paper, the numerical calculations of the optical excitations of the chiral edge states as well as the bulk states in the conduction and valence bands are based on the discrete tight-binding model.

III. OPTICAL GENERATION OF SPIN AND VALLEY CURRENTS

Applying the Heisenberg equation of motion and relaxation-time approximation that describe the scattering of excited quantum states, we obtain the generalized semiconductor Bloch equations [26,32]

$$i\hbar \partial_t \rho_{k_y n, k'_y n'}(t) = [\rho(t), H]_{k_y n, k'_y n'} - \Gamma_{k_y n, k'_y n'} \times [\rho_{k_y n, k'_y n'}(t) - \rho_{k_y n, k'_y n'}^{(0)}] \quad (9)$$

where $\rho_{k_y n, k'_y n'}^{(0)}$ is the equilibrium Fermi-Dirac distribution, and $\Gamma_{k_y n, k'_y n'}$ is the relaxation rate for each matrix element of the density matrix. The equilibrium Fermi-Dirac distribution is a function of the temperature being assumed to be $T = 300 \text{ K}$ in our calculation, and of the Fermi level E_F of graphene. The relaxation rates have been theoretically calculated [32] and experimentally measured [35,36]. In this paper, the relaxation rates are constant parameters that are extracted from the references. For diagonal matrix elements, the relaxation rates are all assumed to be $\Gamma = 1/80 \text{ fs}^{-1}$, which is originated from the electron-electron scattering. Because the bandwidth of the system is smaller than the energy level of the optical phonon, 0.2 eV , the relaxation originated from the electron-phonon scattering is neglected. For nondiagonal matrix elements, the relaxation rates are the summation of the diagonal relaxation rate with the off-diagonal dephasing rate that is assumed to be $1/500 \text{ fs}^{-1}$. For the investigation of the second-order nonlinear optical effects, the perturbation solution of the generalized semiconductor Bloch equations up to second order is needed. The density matrix $\rho = \rho^{(0)} + \rho^{(1)} + \rho^{(2)}$. The first-order perturbation solution is

given as

$$\rho_{k_y n, k'_y n'}^{(1)} = (\rho_{k_y n, k_y n}^{(0)} - \rho_{k'_y n', k'_y n'}^{(0)}) \times \sum_{\kappa=\pm 1} \frac{H_{I, k_y n, k'_y n'}^\kappa e^{-i\kappa\omega t}}{\epsilon_{k_y n} - \epsilon_{k'_y n'} - \kappa\hbar\omega - i\Gamma_{k_y n, k'_y n'}} \quad (10)$$

where $\epsilon_{k_y n}$ is the eigenenergy of the corresponding quantum state $|k_y n\rangle$. We denote the solution as $\rho_{k_y n, k'_y n'}^{(1)} = \rho_{k_y n, k'_y n'}^{(1), \kappa=1} e^{-i\omega t} + \rho_{k_y n, k'_y n'}^{(1), \kappa=-1} e^{i\omega t}$ for convenience. The second-order perturbation solution contains zero harmonic and second-harmonic oscillation terms. The optical generation of the direct current is originated from the zero harmonic solution, which is given as

$$\rho_{k_y n, k'_y n'}^{(2)} = \sum_{k''_y n''} \sum_{\kappa=\pm 1} \left[\frac{H_{I, k_y n, k''_y n''}^{-\kappa} \rho_{k''_y n'', k'_y n'}^{(1), \kappa}}{\epsilon_{k_y n} - \epsilon_{k'_y n'} - i\Gamma_{k_y n, k'_y n'}} - \frac{\rho_{k_y n, k''_y n''}^{(1), \kappa} H_{I, k''_y n'', k'_y n'}^{-\kappa}}{\epsilon_{k_y n} - \epsilon_{k'_y n'} - i\Gamma_{k_y n, k'_y n'}} \right]. \quad (11)$$

According to the property of the interaction Hamiltonian, the first- and second-order density matrices satisfy $\rho_{k_y n, k'_y n'}^{(1), \kappa} \propto \delta(-k_y + k'_y + \kappa q_y)$ and $\rho_{k_y n, k'_y n'}^{(2)} \propto \delta(-k_y + k'_y)$. Because the intervalley scattering is neglected, the density matrix is reduced to the direct sum of matrices of K and K' valley, $\rho = \rho^K \oplus \rho^{K'}$.

Since the chiral edge states only carry current along the line defect direction, or \hat{y} , we limit our calculation of the current along the y direction. The current of the K (K') valley can be calculated by taking the expectation value of the momentum operator, $\text{tr}(\rho \hat{j}_y)$, that is,

$$J_y^{K(K')} = \frac{e_0}{L_y m_0} \sum_{k_y n, k'_y n'} \langle k_y n | \hat{p}_y - e_0 A_y | k'_y n' \rangle \rho_{k'_y n', k_y n}^{K(K')} \quad (12)$$

where $\hat{p}_y = -i\hbar \partial_y$ is the y component of the momentum operator, $A_y = -\int E_y dt$ is the vector potential of the optical field, and L_y is the normalization length in the y direction. The matrix elements of $\hat{p}_y - e_0 A_y$ under the atomic orbital basis are first calculated, and then are transferred into the matrix elements under the basis of the noninteracting tight-binding eigenstates [32–34]. The current consists of the canonical current and the gauge current. The canonical current is given by the part of the summation related to \hat{p}_y , and the gauge current is given by the part of the summation related to $-e_0 A_y$. Because the system preserves the lattice translational symmetry along the y direction, the quantum states are the eigenstates of \hat{p}_y , i.e., $|k_y n\rangle \propto e^{ik_y y}$. As a result, we have $\langle k_y n | \hat{p}_y | k'_y n' \rangle \propto \delta(-k_y + k'_y)$. Thus, the canonical current is proportional to the summation $\sum_{k_y n, n'} \langle k_y n | \hat{p}_y | k'_y n' \rangle \rho_{k'_y n', k_y n}^{K(K')}$. The canonical current consists of the intraband (interband) current given by the part of the summation with $n = n'$ ($n \neq n'$). The direct current from the photogalvanic effect and plasmon drag effect is given by the second-order density matrix, so only $\rho^{(2)}$ is involved. For the photogalvanic effect with normally incident optical field, A_y is a spatial constant that can be extracted out of the matrix element. Thus, the gauge current is proportional

to A_y , and thus is a linear response to A_y . For the plasmon drag effect, the evanescent field includes a spatial phase factor, i.e., $A_y \propto e^{ik_y y}$. Therefore, the matrix elements $\langle k_y n | A_y | k'_y n' \rangle$ are proportional to $\delta(-k_y + k'_y + \kappa q_y)$. As a result, only the first-order density matrix contributes to the gauge current. Because both A_y and $\rho^{(1)}$ are proportional to the strength of the optical electric field $|\mathbf{E}_0|$, the gauge current is proportional to $|\mathbf{E}_0|^2$. Thus, the gauge current contributes to the second-order response, which is the plasmon drag direct current.

The magnitudes of the canonical current and the gauge current are estimated by neglecting the detail of the tight-binding wave functions. The magnitudes of the matrix elements of the interaction Hamiltonian are $\langle H_I \rangle \approx m_{C-C} \hbar e_0 |\mathbf{E}| / (2m_0 \omega)$. The magnitudes of the matrix elements of \hat{p}_y and $e_0 A_y$ are $\langle \hat{p}_y \rangle \approx \hbar m_{C-C}$ and $\langle e_0 A_y \rangle \approx e_0 |\mathbf{E}| / \omega$, respectively. $\rho^{(1)}$ is dominated by the summation terms with $\hbar \omega$ being resonant to the transition, so that $\rho^{(1)} \approx \langle H_I \rangle / \Gamma$. According to the definition of the gauge current, its magnitude is given as $e_0 |\mathbf{E}| \langle H_I \rangle / (\omega \Gamma)$. The summation for the intraband canonical current includes the diagonal elements of $\rho^{(2)}$ with the denominator being $-i\Gamma$, while the summation of the interband canonical current includes the nondiagonal elements of $\rho^{(2)}$ with a larger denominator. Thus, the canonical current mainly consists of the intraband current, the magnitude of which is $\hbar m_{C-C} (\langle H_I \rangle / \Gamma)^2$. The ratio between the canonical current and gauge current is $m_{C-C}^2 \hbar^2 / (2m_0 \Gamma) \approx 41$, so that the magnitude of the canonical current is much larger than that of the gauge current. The numerical result from calculating Eq. (12) shares the same conclusion that the canonical current is two orders of magnitude larger than the gauge current. Hereafter only the canonical current will be discussed.

The canonical current consists of the localized chiral current and bulk current. The localized chiral current of valley K (K') is defined as

$$\begin{aligned} J_{y,c}^{K(K')} &= \frac{e_0}{L_y m_0} \sum_{k_y}^{n,n' \in \text{chiral}} \langle k_y n | \hat{p}_y | k_y n' \rangle \rho_{k_y n', k_y n}^{(2), K(K')} \\ &+ \frac{e_0}{L_y m_0} \sum_{k_y, n' \in \text{bulk}}^{n \in \text{chiral}} \langle k_y n | \hat{p}_y | k_y n' \rangle \rho_{k_y n', k_y n}^{(2), K(K')} \\ &+ \frac{e_0}{L_y m_0} \sum_{k_y, n' \in \text{chiral}}^{n \in \text{bulk}} \langle k_y n | \hat{p}_y | k_y n' \rangle \rho_{k_y n', k_y n}^{(2), K(K')}, \quad (13) \end{aligned}$$

which consists of the intraband current of the chiral band and the interband current due to transition between the chiral band and other bands. The bulk current is defined as

$$J_{y,b}^{K(K')} = \frac{e_0}{L_y m_0} \sum_{k_y}^{n,n' \in \text{bulk}} \langle k_y n | \hat{p}_y | k_y n' \rangle \rho_{k_y n', k_y n}^{(2), K(K')}, \quad (14)$$

which consists of the intraband current of bulk bands and the interband current due to transition between two bulk bands. Assuming the bulk current has uniform distribution in the x direction, the line current density is obtained as $j_{y,b}^{K(K')} = J_{y,b}^{K(K')} / L_x$, with L_x being the width of the nanoribbon. The wave function of a chiral edge state has an exponential decay factor as shown in Fig. 3(a). Because the Rashba SOC is weak, the exponential decay factor could be approximated

as $e^{-\Delta_0 |x| / (\hbar v_F)}$, which is the analytical solution without the Rashba SOC. Thus, the spatial density of the localized chiral current has a factor $e^{-2\Delta_0 |x| / (\hbar v_F)}$. Since the current is obtained by integrating the current density, the current density at the line defect is given as $j_{y,c}^{K(K')} = J_{y,c}^{K(K')} \Delta_0 / (\hbar v_F)$. In the discrete model for the numerical calculation, the width of the nanoribbon is $L_x = 511.2$ nm. On the other hand, the characteristic width of the spatial density of the chiral edge states is $\hbar v_F / \Delta_0 = 21.4$ nm $\ll L_x$. Therefore, the magnitude of the ratio between $j_{y,c}^{K(K')}$ and $j_{y,b}^{K(K')}$ at the line defect is much larger than that between $J_{y,c}^{K(K')}$ and $J_{y,b}^{K(K')}$. For valleytronic and spintronic devices, extraction of current of the nanoribbon is more feasible than extraction of current density, so that our remaining calculations and discussions will be concentrated on the currents defined in Eqs. (13) and (14).

The charge current from either chiral edge states or bulk states is the summation of currents from two valleys, $J_{y,c(b)}^C = J_{y,c(b)}^K + J_{y,c(b)}^{K'}$. The valley current is the subtraction of the currents from two valleys, $J_{y,c(b)}^V = J_{y,c(b)}^K - J_{y,c(b)}^{K'}$. The spin current, denoted as $J_{y,c(b)}^S$, can be obtained by calculating the expectation value of the spin current operator $\frac{\hbar}{4m_0} [(\hat{p}_y - e_0 A_y) \mathbf{S} + \mathbf{S}(\hat{p}_y - e_0 A_y)]$. Replacing the current operator in Eq. (12) by the spin current operator, we obtain the spin current of each component of spin. Because the chiral edge states only have a nonzero expectation value of the spin x component, we will calculate the spin current of the spin x component along the y direction, $J_{y,c(b)}^{S_x}$. Similar analysis shows that the gauge spin current is two orders of magnitude smaller than the canonical spin current, so we will only calculate the canonical spin current. For the present interest, only the localized valley and spin currents originated from the chiral edge states are desirable. The system with large magnitude of localized chiral current and small magnitude of bulk current could be found by tuning parameters including ω , \mathbf{q} , and E_F . The localization factors for the valley current, $|J_{y,c}^V / J_{y,b}^V|$, and the spin current, $|J_{y,c}^{S_x} / J_{y,b}^{S_x}|$, quantify the degree of localization of optical generated currents. In some specific parameters the bulk current is zero, and thus one can obtain a purely localized chiral current, as shown in the following numerical result. It is more interesting to generate valley and spin currents while the charge current $J_y^C = J_{y,c}^K + J_{y,c}^{K'} + J_{y,b}^K + J_{y,b}^{K'}$ is vanishing or negligible.

A. Photogalvanic effect

For the system of Fig. 1(b) the normally incident plane wave has electric field $\mathbf{E}(\mathbf{r}, t) = E_0 \hat{\mathbf{e}} e^{-i\omega t} + \text{c.c.}$, where E_0 is the amplitude of the electric field and $\hat{\mathbf{e}}$ is the polarization unit vector in the x - y plane. The amplitude of the typical laser field, $E_0 = 10^{-3}$ V/ μm , is assumed. Because the system preserves centrosymmetry, the total charge current is zero. However, valley and spin currents are nonzero. The currents generated by the incident field with linear polarization along the x axis, i.e., $\hat{\mathbf{e}} = \hat{x}$, exhibit large localization factors. On the other hand, linear polarization along the y axis and circular polarization have small or moderate localization factors. Under the optical excitation with $\hat{\mathbf{e}} = \hat{x}$, with E_F being 0 and 28 meV, the valley current and the spin current along the graphene nanoribbons are plotted vs the incident field frequency in Fig. 4. The

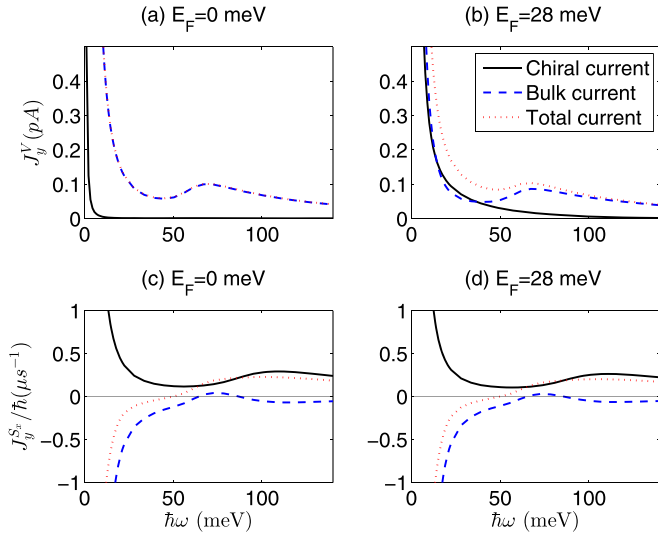


FIG. 4. The valley currents (a), (b) and spin currents (c), (d), which are generated by the photogalvanic effect with the incident field polarization being $\hat{\mathbf{e}}_x$ and the amplitude being $E_0 = 10^{-3}$ V/ μm , vs frequency of the incident field. (a), (c) Intrinsic graphene with $E_F = 0$. (b), (d) Graphene with $E_F = 28$ meV. The legend in figure (b) defines the corresponding line types for the localized chiral currents $J_{y,c}$, bulk currents $J_{y,b}$, and total currents, which applies to all four subfigures.

localized chiral current, bulk current, and total current are plotted as black (solid), blue (dashed), and red (dotted) lines, respectively. The numerical results exhibit a few properties of the valley current and spin current.

(i) In the low-frequency range, $\hbar\omega < \Gamma$, the intraband canonical current is dominating in the localized chiral current and the bulk currents. The valley current and the spin current are proportional to ω^{-2} , which agree with the theoretical estimation for the magnitude of the canonical current. Since the bulk currents do not vanish, the localization factors remain low.

(ii) The trend of the bulk currents is determined by multiple physical processes, which become more complicated than the bulk current of a homogeneous gapped graphene without the line defect. With frequency being larger than the band gap of bulk states, $\hbar\omega > 2\Delta_0$, the optical transitions between bulk states of the valence band and the conduction band are allowed, as shown in Fig. 5(a), that gives significant contribution to the bulk currents. Because of the reflection and transmission of the bulk states at the line defect, the wave functions in the homogeneous regions far away from the line defect indicate superposition of multiple Bloch states, which change the strength and phase of the optical transition of each channel. In addition, the optical transitions from the chiral bands to the bulk bands partially determine the second-order density-matrix elements of the bulk states, as shown in Eq. (11), which indirectly influence the bulk currents. The combination of these physical processes makes the trend of the bulk currents become bumpy in this frequency range, as shown in all four panels of Fig. 4. The bulk currents vanish in some cases, as shown in the following properties.

(iii) In the frequency range of $\hbar\omega > \Gamma$, for the case of intrinsic graphene with $E_F = 0$, the localized valley current

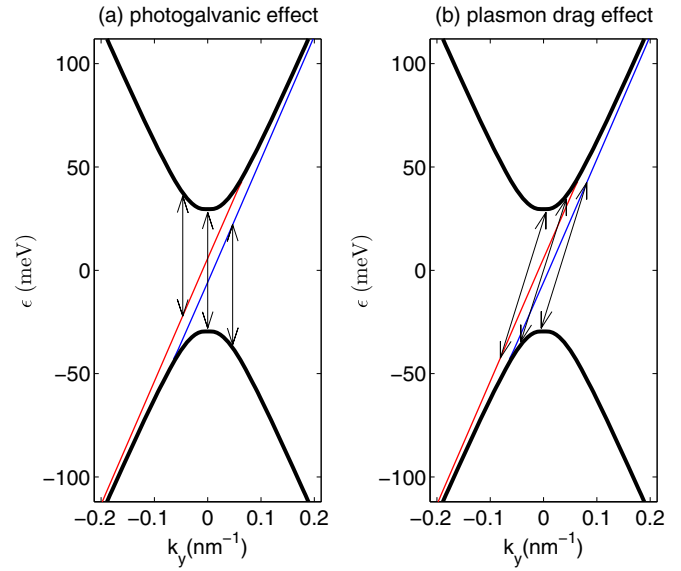


FIG. 5. The interband optical transition channels among the bulk bands as well as between the bulk bands and the chiral bands, plotted as double arrows. The conduction- and valence-band edges are denoted by the thick black lines, and the chiral bands are denoted by the thin blue and red lines. The minimal frequency of the incident field for transition between the conduction and valence bulk bands in the photogalvanic effect (a) is the band gap of the bulk bands, $2\Delta_0$; that in the plasmon drag effect (b) is 69 meV $> 2\Delta_0$, because of the momentum transfer from the SPs to the electrons.

is weakly excited, as shown in Fig. 4(a). When the Fermi level is tuned to $E_F = 28$ meV, the localized valley current is significantly enhanced, but the bulk valley current is not suppressed, so that the localization factor is still low, as shown in Fig. 4(b). Tuning the Fermi level to a negative value does not suppress the bulk valley current either.

(iv) In the frequency range of $\hbar\omega > \Gamma$, the localized spin currents and bulk spin currents have the same order of magnitude. With the frequencies of the incident field being 65 and 86 meV, the bulk spin currents equate to zero, so that the optically generated spin current is purely localized, as shown in Fig. 4(c). Tuning the Fermi level weakly affects the spin current, as shown in Fig. 4(d).

B. Plasmon drag effect

Now we turn to the system of Fig. 1(c) where the evanescent field of the SP is induced by obliquely incident light with the electric field $\mathbf{E}(\mathbf{r}, t) = E_0 \hat{\mathbf{q}} e^{i\mathbf{q}\cdot\mathbf{r} - i\omega t} + \text{c.c.}$, where E_0 is the amplitude of the electric field and $\hat{\mathbf{q}}$ is the unit vector along \mathbf{q} . Note that the evanescent field of the SPs has TM polarization only, so that the electric field has $\hat{\mathbf{q}}$ and $\hat{\mathbf{z}}$ components. Because the π electrons are tightly bound along the $\hat{\mathbf{z}}$ direction, the excitation by the $\hat{\mathbf{z}}$ component electric field is neglected. The frequency ω and the wave number $|\mathbf{q}|$ of the SPs in the plasmonic layer satisfy the dispersive relation $\omega \propto \sqrt{n_{\text{SP}}|\mathbf{q}|}$ [37], with n_{SP} being the surface charge density of the plasmonic layer. For a given wave number $|\mathbf{q}|$, tuning n_{SP} by gating or doping one obtains SPs of various frequencies. We only consider the case that the SP propagates

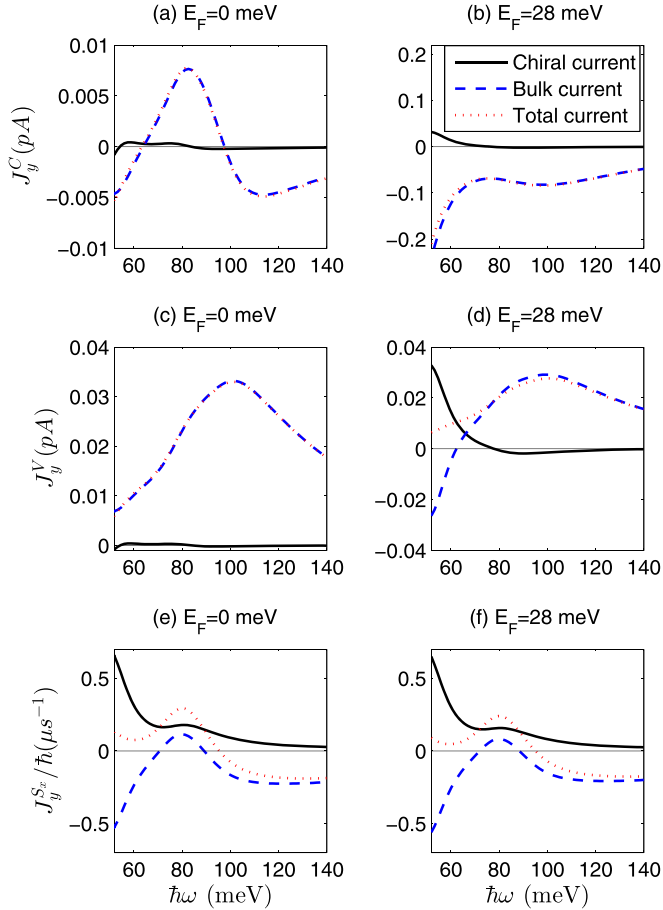


FIG. 6. The charge currents (a), (b), valley currents (c), (d), and spin currents (e), (f), which are generated by the plasmon drag effect with the incident field wave number being $|\mathbf{q}| = 0.085 \text{ nm}^{-1}$ and the amplitude being $E_0 = 10^{-3} \text{ V}/\mu\text{m}$, vs frequency of the incident field. (a), (c), (e) Intrinsic graphene with $E_F = 0$. (b), (d), (f) Graphene with $E_F = 28 \text{ meV}$. The legend in figure (b) applies to all six subfigures.

along the line defect, i.e., $\hat{\mathbf{q}} = \hat{\mathbf{y}}$. Thus, the tunable parameters of this optical excitation system are $|\mathbf{q}|$ and ω , as well as E_F . In our calculation, the plasmonic layer is a doped graphene [38]. In this case, the minimal frequency of the SPs is $\hbar v_F |\mathbf{q}|$, because the SPs with frequency lower than this value are highly lossy and not suitable as a light source for the plasmon drag effect. The phase factor of the electromagnetic field breaks the centrosymmetry of the system, so that the SP excitation could induce charge current. As an example, the plasmon drag effect with $|\mathbf{q}| = 0.085 \text{ nm}^{-1}$ is plotted in Fig. 6, which presents plasmon drag inducing charge current, valley current, and spin current with the Fermi level being 0 and 28 meV in six panels separately. The minimal frequency for the interband SP transition between the valence and conduction bulk bands is 69 meV, as shown in Fig. 5(b), which is larger than the band gap of the bulk states because of the momentum transfer from the SPs to the electrons. Thus, in the frequency range $\omega > 69 \text{ meV}$, these transitions contribute to the bulk currents and suppress the bulk currents to zero in some cases. The numerical result gives a few remarkable sets of parameters as follows:

(i) When the graphene Fermi level is zero, the total charge current maintains small magnitude or vanishes with

the incident field frequencies being 64 and 97 meV, as shown in Fig. 6(a). With the Fermi level deviated from zero, the magnitude of the total charge current increases, as shown in Fig. 6(b).

(ii) For the case of intrinsic graphene, $E_F = 0$, the localized valley current is much smaller than the bulk valley current, as shown in Fig. 6(c). When the Fermi level is tuned to $E_F = 28 \text{ meV}$, the bulk valley current equates to zero with the incident field frequencies being 62 meV, as shown in Fig. 6(d). This gives an instance of purely localized valley current.

(iii) For the case of intrinsic graphene, $E_F = 0$, the bulk spin current equates to zero with the incident field frequency being 71 or 89 meV, as shown in Fig. 6(e). Tuning the Fermi level to $E_F = 28 \text{ meV}$ hardly changes the spin current, as shown in Fig. 6(f). This is an instance of the purely localized spin current.

Thus the plasmon drag effect can generate purely localized valley or spin currents at certain sets of parameters. Because the total charge current has small or vanishing magnitude in graphene with zero Fermi level, the purely localized spin current may be observed easily in intrinsic graphene. The localized valley current exists in the system with a nonzero graphene Fermi level, which is accompanied with large magnitude of the total charge current. So this system is less favorable for observation of the localized valley current.

With different values of $|\mathbf{q}|$, the purely localized valley current and spin current appear at different frequencies of the incident field. When $|\mathbf{q}|$ is smaller than 0.053 nm^{-1} , the bulk valley current and bulk spin current remain finite for all frequencies and Fermi levels, and therefore the purely localized valley current and spin current are not available in this case.

IV. CONCLUSION

In summary, we investigated the chiral edge states of monolayer graphene on the h-BN substrate, which is localized near to the topological line defect of the substrate (B-B or N-N line) along the zigzag edge, with both the continuous Dirac fermion model and discrete tight-binding model. In the presence of the Rashba SOC, the linear dispersion of the chiral edge states splits into two branches. The spin x components of the chiral edge states of two branches have opposite signs. Based on the discrete tight-binding model, generalized semiconductor Bloch equations are developed to describe the optical excitation of the chiral edge states as well as the bulk states. The optical generation of charge, valley, and spin currents, including the localized chiral currents originated from the chiral edge states and the bulk currents originated from the bulk states, are calculated. With normally incident optical field, the localized and bulk currents coexist in general. However, at certain frequencies of the incident field, the bulk spin current vanishes and the optically excited current is a purely localized chiral current. With the evanescent field of the SP, the localized and bulk currents also coexist in general. However, there are also certain combinations of the incident field frequency and wave number as well as the graphene Fermi level that lead to vanishing bulk valley or spin current. As a result, the purely localized valley or spin current is obtainable under certain

conditions with either photogalvanic effect or plasmon drag effect. Manipulation of the purely localized valley or spin current could become feasible. Thus, our theoretical result may lead to integrated optical spintronic and valleytronic devices. The model can be improved by including time-dependent optical excitation and detailed description of the scattering processes.

ACKNOWLEDGMENTS

The project is supported by the National Natural Science Foundation of China (Grants No. 11274393 and No. 11704419), the National Basic Research Program of China (Grant No. 2013CB933601), and the National Key Research and Development Project of China (Grant No. 2016YFA0202000).

-
- [1] W. Han, R. K. Kawakami, M. Gmitra, and J. Fabian, *Nat. Nanotechnol.* **9**, 794 (2014).
- [2] J. R. Schaibley, H. Yu, G. Clark, P. Rivera, J. S. Ross, K. L. Seyler, W. Yao, and X. Xu, *Nat. Rev. Mater.* **1**, 16055 (2016).
- [3] J. Li and P. M. Haney, *Phys. Rev. B* **93**, 155432 (2016).
- [4] H. Min, J. E. Hill, N. A. Sinitsyn, B. R. Sahu, L. Kleinman, and A. H. MacDonald, *Phys. Rev. B* **74**, 165310 (2006).
- [5] D. Huertas-Hernando, F. Guinea, and A. Brataas, *Phys. Rev. B* **74**, 155426 (2006).
- [6] J. C. Boettger and S. B. Trickey, *Phys. Rev. B* **75**, 121402(R) (2007).
- [7] A. H. C. Neto, F. Guinea, N. M. R. Peres, K. S. Novoselov, and A. K. Geim, *Rev. Mod. Phys.* **81**, 109 (2009).
- [8] D. N. Basov, M. M. Fogler, A. Lanzara, F. Wang, and Y. Zhang, *Rev. Mod. Phys.* **86**, 959 (2014).
- [9] M. Inglot, V. K. Dugaev, E. Ya. Sherman, and J. Barnas, *Phys. Rev. B* **89**, 155411 (2014).
- [10] J. Rioux and G. Burkard, *Phys. Rev. B* **90**, 035210 (2014).
- [11] M. Inglot, V. K. Dugaev, E. Ya. Sherman, and J. Barnas, *Phys. Rev. B* **91**, 195428 (2015).
- [12] V. Kaladzhyan, P. P. Aseev, and S. N. Artemenko, *Phys. Rev. B* **92**, 155424 (2015).
- [13] L. E. Golub, S. A. Tarasenko, M. V. Entin, and L. I. Magarill, *Phys. Rev. B* **84**, 195408 (2011).
- [14] W.-Yu. Shan, J. Zhou, and D. Xiao, *Phys. Rev. B* **91**, 035402 (2015).
- [15] G. W. Semenoff, V. Semenoff, and F. Zhou, *Phys. Rev. Lett.* **101**, 087204 (2008).
- [16] M. Zarenia, O. Leenaerts, B. Partoens, and F. M. Peeters, *Phys. Rev. B* **86**, 085451 (2012).
- [17] D. R. da Costa, A. Chaves, M. Zarenia, J. M. Pereira, Jr., G. A. Farias, and F. M. Peeters, *Phys. Rev. B* **89**, 075418 (2014).
- [18] M. M. Grujic, M. Z. Tadic, and F. M. Peeters, *Phys. Rev. B* **91**, 245432 (2015).
- [19] M. Pelc, W. Jaskolski, A. Ayuela, and L. Chico, *Phys. Rev. B* **92**, 085433 (2015).
- [20] L. Cohnitz, A. De Martino, W. Hausler, and R. Egger, *Phys. Rev. B* **94**, 165443 (2016).
- [21] S. Y. Zhou, G.-H. Gweon, A. V. Fedorov, P. N. First, W. A. de Heer, D.-H. Lee, F. Guinea, A. H. C. Neto, and A. Lanzara, *Nat. Mater.* **6**, 770 (2007).
- [22] C. R. Dean, A. F. Young, I. Meric, C. Lee, L. Wang, S. Sorgenfrei, K. Watanabe, T. Taniguchi, P. Kim, K. L. Shepard, and J. Hone, *Nat. Nanotechnol.* **5**, 722 (2010).
- [23] E. I. Rashba, *Phys. Rev. B* **79**, 161409(R) (2009).
- [24] M. Zarea and N. Sandler, *Phys. Rev. B* **79**, 165442 (2009).
- [25] H. Santos, A. Latge, J. E. Alvarillos, and L. Chico, *Phys. Rev. B* **93**, 165424 (2016).
- [26] M. Luo and Z. Li, *Phys. Rev. B* **94**, 235435 (2016).
- [27] Z. Qiao, S. A. Yang, W. Feng, W.-K. Tse, J. Ding, Y. Yao, J. Wang, and Q. Niu, *Phys. Rev. B* **82**, 161414(R) (2010).
- [28] C. Weeks, J. Hu, J. Alicea, M. Franz, and R. Wu, *Phys. Rev. X* **1**, 021001 (2011).
- [29] J. Ding, Z. Qiao, W. Feng, Y. Yao, and Q. Niu, *Phys. Rev. B* **84**, 195444 (2011).
- [30] G. Giovannetti, P. A. Khomyakov, G. Brocks, P. J. Kelly, and J. van den Brink, *Phys. Rev. B* **76**, 073103 (2007).
- [31] D. Kochan, S. Irmer, and J. Fabian, *Phys. Rev. B* **95**, 165415 (2017).
- [32] E. Malic, T. Winzer, E. Bobkin, and A. Knorr, *Phys. Rev. B* **84**, 205406 (2011).
- [33] H. Hsu and L. E. Reichl, *Phys. Rev. B* **76**, 045418 (2007).
- [34] A. K. Gupta, O. E. Alon, and N. Moiseyev, *Phys. Rev. B* **68**, 205101 (2003).
- [35] M. Breusing, S. Kuehn, T. Winzer, E. Malic, F. Milde, N. Severin, J. P. Rabe, C. Ropers, A. Knorr, and T. Elsaesser, *Phys. Rev. B* **83**, 153410 (2011).
- [36] D. Brida, A. Tomadin, C. Manzoni, Y. J. Kim, A. Lombardo, S. Milana, R. R. Nair, K. S. Novoselov, A. C. Ferrari, G. Cerullo, and M. Polini, *Nat. Commun.* **4**, 1987 (2013).
- [37] J. M. Pitarke, V. M. Silkin, E. V. Chulkov, and P. M. Echenique, *Rep. Prog. Phys.* **70**, 1 (2007).
- [38] M. Jablan, M. Soljacic, and H. Buljan, *Proc. IEEE* **101**, 1689 (2013).